

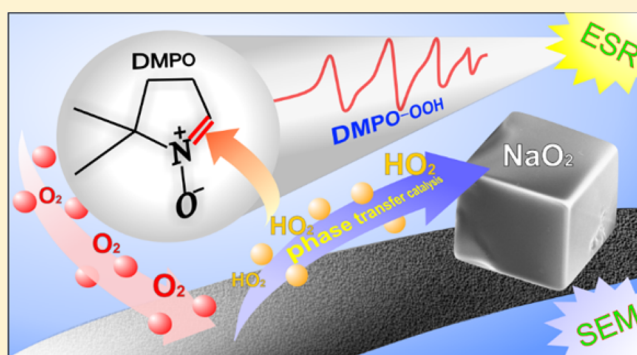
# Direct Evidence of Solution-Mediated Superoxide Transport and Organic Radical Formation in Sodium-Oxygen Batteries

Chun Xia,<sup>†,‡</sup> Russel Fernandes,<sup>†,‡</sup> Franklin H. Cho,<sup>§,||</sup> Niranjan Sudhakar,<sup>‡</sup> Brandon Buonacorsi,<sup>§,||</sup> Sean Walker,<sup>†,§</sup> Meng Xu,<sup>†,‡</sup> Jonathan Baugh,<sup>\*,†,‡,§</sup> and Linda F. Nazar<sup>\*,†,‡,||</sup>

<sup>†</sup>Department of Chemistry, <sup>§</sup>Institute for Quantum Computing, <sup>||</sup>Department of Physics and Astronomy, and <sup>‡</sup>Waterloo Institute for Nanotechnology, University of Waterloo, Waterloo Ontario N2L 3G1, Canada

**S** Supporting Information

**ABSTRACT:** Advanced large-scale electrochemical energy storage requires cost-effective battery systems with high energy densities. Aprotic sodium-oxygen (Na-O<sub>2</sub>) batteries offer advantages, being comprised of low-cost elements and possessing much lower charge overpotential and higher reversibility compared to their lithium-oxygen battery cousins. Although such differences have been explained by solution-mediated superoxide transport, the underlying nature of this mechanism is not fully understood. Water has been suggested to solubilize superoxide via formation of hydroperoxyl (HO<sub>2</sub>), but direct evidence of these HO<sub>2</sub> radical species in cells has proven elusive. Here, we use ESR spectroscopy at 210 K to identify and quantify soluble HO<sub>2</sub> radicals in the electrolyte—cold-trapped *in situ* to prolong their lifetime—in a Na-O<sub>2</sub> cell. These investigations are coupled to parallel SEM studies that image crystalline sodium superoxide (NaO<sub>2</sub>) on the carbon cathode. The superoxide radicals were spin-trapped via reaction with 5,5-dimethyl-pyrroline N-oxide at different electrochemical stages, allowing monitoring of their production and consumption during cycling. Our results conclusively demonstrate that transport of superoxide from cathode to electrolyte leads to the nucleation and growth of NaO<sub>2</sub>, which follows classical mechanisms based on the variation of superoxide content in the electrolyte and its correlation with the crystallization of cubic NaO<sub>2</sub>. The changes in superoxide content upon charge show that charge proceeds through the reverse solution process. Furthermore, we identify the carbon-centered/oxygen-centered alkyl radicals arising from attack of these solubilized HO<sub>2</sub> species on the diglyme solvent. This is the first direct evidence of such species, which are likely responsible for electrolyte degradation.



## INTRODUCTION

It is well recognized that the electrification of transportation would minimize the consumption of fossil fuels and reduce CO<sub>2</sub> emissions. Similarly, electrochemical energy storage allows for intermittent renewable energy sources such as wind and solar to become dispatchable. The key to realize these very important aims relies on cost-effective batteries with high energy densities and good cyclability.<sup>1</sup> Although lithium-ion batteries greatly satisfy the needs of small mobile devices, e.g., cell phones, their low energy densities (typically between 100 to 200 Wh kg<sup>-1</sup>) cannot effectively meet the demands of high-energy, large-scale storage at very low cost.<sup>2</sup>

Metal-air batteries have attracted considerable attention in the search for rechargeable batteries with superior energy densities and a potentially lower price point. In contrast to the intercalation chemistry of conventional lithium-ion batteries, nonaqueous alkali metal-air batteries utilize oxygen derived from air to form alkali metal oxides upon discharge and reversibly evolve oxygen during charge.<sup>3</sup> Nonaqueous lithium-air batteries (more properly known as Li-O<sub>2</sub> cells), first discovered in 1996, possess a very high theoretical energy

density of 3500 Wh kg<sup>-1</sup>, which is a magnitude higher than current lithium-ion batteries.<sup>4</sup> It is the highest energy per unit mass of any electrochemical storage system. However, major fundamental and technological challenges still remain for Li-O<sub>2</sub> batteries.<sup>5,6</sup> The oxidation of the insulating Li<sub>2</sub>O<sub>2</sub> products upon charge leads to a high overpotential (typically above 1 V).<sup>7,8</sup> This results in a poor round-trip energy storage efficiency and, more importantly, rapid capacity decay during cycling.<sup>9</sup> To overcome this hurdle, recent work has focused on the use and development of redox mediators.<sup>10,11</sup> The aprotic electrolytes used in Li-O<sub>2</sub> cells, such as ether-based electrolytes, undergo decomposition during discharge.<sup>12</sup> Moreover, the carbon cathodes become chemically corroded by Li<sub>2</sub>O<sub>2</sub> at the Li<sub>2</sub>O<sub>2</sub>/carbon interface because of the high voltage needed to overcome the overpotential.<sup>13,14</sup> These undesired side reactions result in the formation of byproducts, e.g., lithium carbonate and carboxylate, which greatly reduce the reversibility of Li-O<sub>2</sub> cells.<sup>15,16</sup> Recently, reversible Li-O<sub>2</sub> cells based on LiOH

Received: May 25, 2016

Published: August 7, 2016

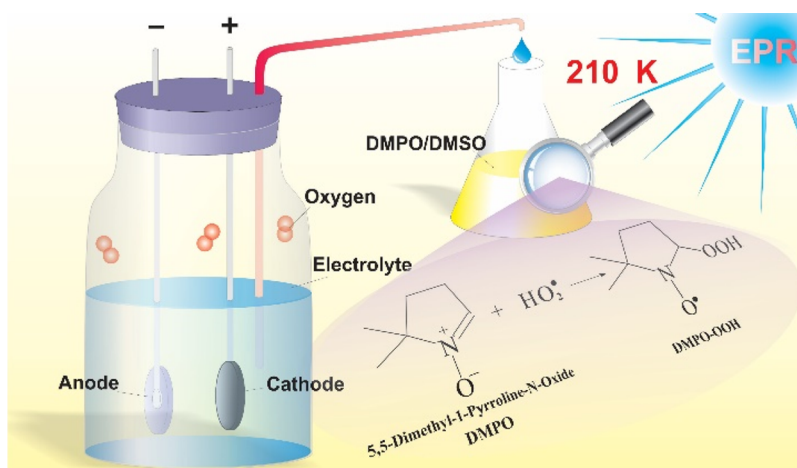


**Figure 1.** Schematic illustration of the Na-O<sub>2</sub> cell and *in situ* electrolyte extraction during cycling to spin-trap either HO<sub>2</sub> radicals as the DMPO-OOH adducts at 210 K and/or carbon based radicals. The low temperature stabilizes the radicals and allows their study by ESR spectroscopy.

products using reduced graphene oxide and lithium iodide as the cathode/redox mediator, respectively,<sup>17</sup> or Ru/MnO<sub>2</sub> as the “catalyst” in the presence of trace water<sup>18</sup> have been reported. However, the mechanism is still not well-understood.

In contrast, nonaqueous sodium-air batteries (also known as Na-O<sub>2</sub> cells) present more reversible chemistry, as demonstrated by Hartman et al., when sodium superoxide (NaO<sub>2</sub>) is produced as the main discharge product using a “dry” diglyme-based electrolyte.<sup>19</sup> Although Na-O<sub>2</sub> cells offer a lower theoretical energy density (1105 Wh kg<sup>-1</sup> based on NaO<sub>2</sub>) than Li-O<sub>2</sub> cells, they feature a much more abundant, sustainable element—Na—and a much lower charge overpotential (typically below 0.2 V) and better rechargeability.<sup>20</sup> Such differences are partly due to their discharge products that are stabilized as NaO<sub>2</sub>, which does not spontaneously disproportionate to sodium peroxide (Na<sub>2</sub>O<sub>2</sub>).<sup>21</sup> Lu et al. described a Li-O<sub>2</sub> cell based on lithium superoxide (instead of Li<sub>2</sub>O<sub>2</sub>) which shows a similar low charge overpotential,<sup>22</sup> as does the recently reported K-O<sub>2</sub> cell where KO<sub>2</sub> is formed as the discharge product.<sup>23</sup> The deeper understanding into the formation and oxidation mechanisms of NaO<sub>2</sub> described in this report reveals why Na-O<sub>2</sub> cells possess such different electrochemical characteristics and helps identify issues in other alkali metal-oxygen chemistry, such as Li-O<sub>2</sub> and K-O<sub>2</sub>. These relate to the organic radical chemistry that characterizes these aprotic systems.

Upon discharge of a Na-O<sub>2</sub> cell, NaO<sub>2</sub> products are deposited as micrometer-sized cubic crystals. There has been much speculation on the mechanisms of crystal growth and two pathways have been put forward.<sup>24</sup> The first pathway suggests that NaO<sub>2</sub> possesses sufficient electronic conductivity to allow oxygen to be directly reduced on its surface, leading to the electrochemical growth of NaO<sub>2</sub> crystals. Indeed, Lee et al. reported that the electronic and ionic conductivities were calculated to be significantly higher in superoxide than peroxide.<sup>25</sup> However, recent density functional theory (DFT) calculations and electrochemical atomic force microscopy (AFM) studies by Hartmann et al. demonstrated that pure stoichiometric NaO<sub>2</sub> presents negligible conductivity at room temperature, similar to both Na<sub>2</sub>O<sub>2</sub> and Li<sub>2</sub>O<sub>2</sub>.<sup>26</sup> The “surface conductive” pathway is thus under considerable debate. The second pathway proposes that the transport of superoxide in an ether-based electrolyte results in the nucleation and growth of

NaO<sub>2</sub> particles.<sup>27</sup> Based on thermodynamic calculations, Shao-Horn and Lee concluded that superoxide exhibits much lower nucleation and dissolution energies than peroxide, which theoretically allows the growth of NaO<sub>2</sub> crystals through solution processes.<sup>25,28</sup> In our previous work, we experimentally demonstrated that the second pathway is operative and driven by the presence of proton phase-transfer catalysts (PPTCs), e.g., water or proton donors such as benzoic acid.<sup>29</sup> A trace amount of H<sub>2</sub>O (<10 ppm) in the electrolyte leads to the formation of cubic NaO<sub>2</sub> crystals and a massive increase in discharge capacity by comparison to a dry electrolyte. In the absence of a PPTC, quasi-amorphous NaO<sub>2</sub> films are formed, delivering negligible cell capacity. The role of water has also been highlighted in Li-O<sub>2</sub> cells, (but at ultrahigh concentrations; a few thousand ppm) which may operate via a different mechanism.<sup>30</sup> We speculated that PPTCs are able to reversibly transfer superoxide from the carbon surface to the incipient NaO<sub>2</sub> crystal nuclei via soluble HO<sub>2</sub> radicals. These are formed by the reaction of a weak acid such as water (HA) with superoxide: HA + O<sub>2</sub><sup>•-</sup> ⇌ HO<sub>2</sub> + A<sup>-</sup>. Metathesis (HO<sub>2</sub> + Na<sup>+</sup> ⇌ NaO<sub>2</sub> + H<sup>+</sup>) is responsible for transport and growth. Our rotating ring-disk electrode (RRDE) studies also showed that H<sub>2</sub>O additives lower the onset overpotential of the oxygen reduction reaction (ORR), leading to much larger ring and disc currents. Although the effects of H<sub>2</sub>O in both Li-O<sub>2</sub> and Na-O<sub>2</sub> cells are becoming better understood, there has been no direct evidence for the soluble hydroperoxyl radical. Research to date has not provided proof of solution-mediated superoxide transport and its dependence on PPTCs. Furthermore, the mechanisms behind the proposed solution-mediated crystal growth and dissolution are not understood.

Here, for the first time, we employ a unique combination of spectroscopic and microscopic techniques to elucidate this complex radical chemistry. We quantify the superoxide species in the electrolyte and on the solid cathode by using coupled electron spin resonance (ESR) spectroscopy and scanning electron microscopy (SEM) studies. Spectra and SEM images were collected in parallel and from *operando* cells as a function of charge passed and equilibration time. Our results unequivocally demonstrate that the superoxide transfers through solution processes and leads to the formation and oxidation of NaO<sub>2</sub>. We show directly, via ESR, that these solubilized superoxide species also attack the aprotic electrolyte

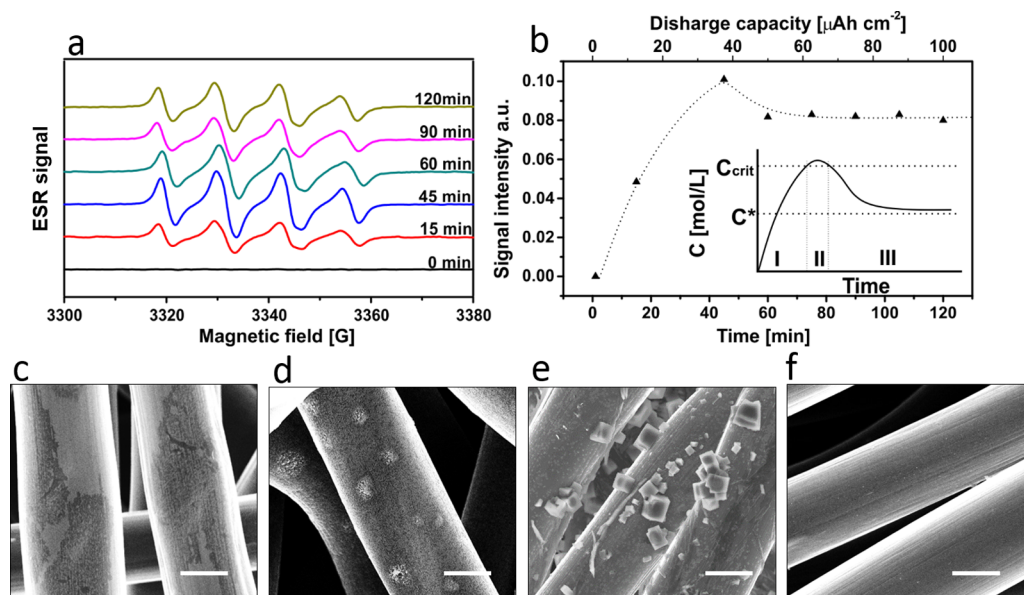


**Figure 2.** X-band ESR spectra of the electrolyte at different discharge depths (a) and the corresponding intensity variation of the DMPO-OOH ESR signal (b). (c–f) SEM images of carbon-fiber cathode discharged for 15 min (c), 90 min (d), 600 min (e), and 15 min followed by immersing the cathode into electrolyte for 1 h (f). The white bars indicate a length of 5  $\mu\text{m}$ . The discharge current is 50  $\mu\text{A cm}^{-2}$ .

leading to the formation of organic radicals. This is the first *in situ* evidence of such species to our knowledge, which is important because such radicals play a crucial role in electrolyte degradation.

## EXPERIMENTAL SECTION

**ESR Spin-Trapping Technique.** ESR, a radical-sensitive spectroscopic technique, paired with 5,5-dimethyl-pyrroline *N*-oxide (DMPO) spin traps, has been used to investigate short-lived superoxide radicals.<sup>31</sup> By forming relatively stable DMPO-OOH adducts (i.e., DMPO- $\text{HO}_2$ ), the solubilized superoxide species can be readily trapped by DMPO, whereas  $\text{NaO}_2$  is obviously not (Figure S1).<sup>32</sup> This allows for ESR investigations of the superoxide species in the electrolyte. Recently Cao et al. performed ESR studies on cathodic reactions in  $\text{Li-O}_2$  cells by adding DMPO directly into the cell.<sup>33</sup> However, the ongoing degradation of DMPO-OOH adducts during discharge at room temperature complicates the resulting ESR spectra and obscures the underlying mechanisms (Figure S2).<sup>34</sup> In our work, 100  $\mu\text{L}$  of electrolyte composed of 0.5 M sodium trifluoromethanesulfonate ( $\text{NaOTf}$ ) in distilled diethylene glycol dimethyl ether (diglyme) was extracted *in situ* from a  $\text{Na-O}_2$  glass cell operating during discharge or charge at various stages of electrochemical cycling and quickly cold-trapped at 210 K via reaction with 500  $\mu\text{L}$  of 0.1 M DMPO in dimethyl sulfoxide (DMSO), as illustrated in Figure 1. The ESR spectrum of the supercooled solution was immediately measured by an X-band continuous-wave (CW) ESR spectrometer at 210 K. This temperature was chosen to suppress side reactions, and hence stabilize all the radicals formed during cycling, and to facilitate tuning of the ESR cavity. The morphological changes of the products at the same points corresponding to the ESR spectral collection were investigated in parallel using a LEO 1530 field-emission SEM, by extraction of the carbon diffusion layer cathode (GDL H2315, Freudenberg). To study the role of water in the cell, varying amounts of deionized water were added into the electrolyte; its precise water concentration was determined by KF titration before use. Full details on the experimental methodology and analysis and simulation of the ESR spectra are given in the Supporting Information.

## RESULTS AND DISCUSSION

**Nucleation and Growth of  $\text{NaO}_2$  from Electrolyte.** Variations in the ESR spectra of the electrolyte and the

morphological changes of the cathodic products upon discharge are shown in Figure 2. The purified electrolyte contains 10 ppm of  $\text{H}_2\text{O}$  (as determined by Karl Fischer titration; see experimental section, SI). Prior to discharge, the pristine electrolyte does not yield an ESR signal. Once ORR commences, a distinct ESR spectrum with four broad peaks appears as shown in Figure 2a. The observed ESR pattern and extracted hyperfine coupling constants ( $\alpha_{\text{N}} = 13.2$  G,  $\alpha_{\text{H}}^{\beta} = 11.0$  G, and  $\alpha_{\text{H}}^{\gamma} = 0.8$  G) are the same as those of the reported DMPO-OOH adduct (see Figure S3 for the detailed analysis of the ESR spectra).<sup>35</sup> This proves the solubilization of superoxide as hydroperoxyl ( $\text{HO}_2$ ) in the diglyme-based electrolyte. As the discharge proceeds, the ESR pattern of the electrolyte remains, whereas its intensity changes indicating a variation of superoxide concentration.

Figure 2b shows that the intensity of the DMPO-OOH signal initially increases to a maximum value at a discharge time of 45 min, followed by a short decrease that eventually reaches steady state. Such time-dependent changes have also been reported in the crystallization of other nanomaterials in solution, e.g., sulfur, silver halide, and magnetite.<sup>36,37</sup> They are described by the classical LaMer mechanism, based on a seminal study that described a reaction system using a plot of a notional reacting species concentration versus time.<sup>38</sup> Based on this mechanism, the curve representing dissolved superoxide content can be divided into three regions as illustrated in the inset of Figure 2b:<sup>39</sup> (I) The solubilization of superoxide in the electrolyte leads to an initial increase of superoxide concentration. (II) once a critical supersaturation,  $C_{\text{crit}}$ , is achieved, the superoxide, in the presence of sodium cations, undergoes “burst-nucleation” forming a large number of solid  $\text{NaO}_2$  nanonuclei, which reduces the concentration of superoxide in solution. Subsequently, there is almost no nucleation occurring due to the low concentration of free superoxide in the electrolyte. (III) The newly formed superoxide moieties steadily diffuse to the nucleation sites of  $\text{NaO}_2$  nanoparticles. This leads to the epitaxial growth of  $\text{NaO}_2$  crystals and stabilizes the concentration of superoxide at a low supersaturation, i.e., slightly



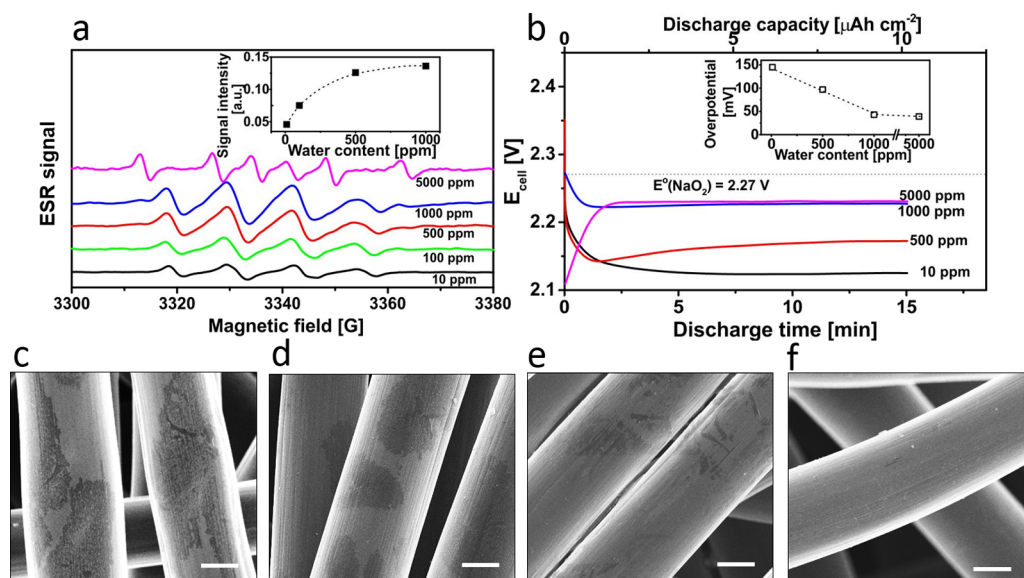


**Figure 3.** Effects of  $\text{H}_2\text{O}$  content on the ESR spectra of discharged electrolytes (a) and the discharge curves of  $\text{Na}-\text{O}_2$  cells at a constant discharge time of 15 min (b). In (b), the electrochemical profile is affected at the highest  $\text{H}_2\text{O}$  concentration of 5000 ppm (magenta) due to reaction of water with the  $\text{Na}$  anode resulting from crossover. Insets: the intensity changes of DMPO-OOH ESR signal and the discharge overpotential changes of cells as a function of  $\text{H}_2\text{O}$  concentration, respectively. (c–f) SEM images of the discharged cathodes using electrolytes with  $\text{H}_2\text{O}$  concentrations of 10 ppm (c), 100 ppm (d), 500 ppm (e), and 1000 ppm (f). The white bars indicate a length of  $5\ \mu\text{m}$ . A constant discharge current of  $50\ \mu\text{A}\ \text{cm}^{-2}$  was applied.

higher than its solubility ( $C^*$ ). The morphology changes of the cathodic products during discharge are shown in Figure 2c–f. At a short discharge time of 15 min (region I), film-like products are formed which partially cover the surface of the carbon fiber cathode (Figure 2c). Such film products are likely to be quasi-amorphous  $\text{NaO}_2$  (Figure S4), which has been previously identified using an almost anhydrous electrolyte.<sup>29</sup> After immersing the cathode in electrolyte for 1 h without polarization, however, the  $\text{NaO}_2$  films are completely dissolved in the electrolyte, revealing the bare surface of the cathode (Figure 2f). This indicates slow dissolution of surface superoxide. Additional experimental evidence is discussed below in the context of Figure 3.<sup>40</sup> Recently, such  $\text{NaO}_2$  thin films have been proven to be highly insulating.<sup>26</sup> They passivate the carbon cathode, reducing the cell capacity, while their oxidation likely causes the initial overpotential feature upon charge. Thus, accelerating the dissolution of superoxide to eliminate the formation of  $\text{NaO}_2$  films is critical to improve the discharge capacity and lower the overall charge overpotential. As the discharge proceeds to 90 min (region III), the entire cathode is covered by a  $\text{NaO}_2$  film. Moreover a number of spot-like particles are found deposited on the cathode (Figure 2d). They are likely to be the  $\text{NaO}_2$  nuclei as predicted by the LaMer mechanism. With a prolonged discharge to 600 min, these  $\text{NaO}_2$  nuclei grow to micrometer-sized  $\text{NaO}_2$  cubic crystals (Figure 2e),<sup>19</sup> kinetically driven by the proton transfer catalytic process. To the best of our knowledge, this is the first experimental observation that conclusively shows that solution-mediated superoxide transport leads to the nucleation and growth of  $\text{NaO}_2$  crystals upon discharge.

**Water-Assisted Superoxide Transfer.** Figure 3 shows the effects of  $\text{H}_2\text{O}$  concentration on the solubilized superoxide species and the morphology of the cathode with a short discharge time of 15 min. With an increase of  $\text{H}_2\text{O}$  content, less  $\text{NaO}_2$  film is found on the cathode (Figure 3c–f). Instead,

more superoxide is detected in the electrolyte that shows enhanced signals of the DMPO-OOH adduct (Figure 3a).

Based on the Noyes–Whitney equation, the poor solubility and low diffusion coefficient of  $\text{NaO}_2$  in the electrolyte with 10 ppm of  $\text{H}_2\text{O}$  likely lead to the slow dissolution of  $\text{NaO}_2$ .<sup>26</sup> However, with the increase of  $\text{H}_2\text{O}$  content, the superoxide anion—being a strong Brønsted base—readily abstracts a proton from  $\text{H}_2\text{O}$ , forming the soluble  $\text{HO}_2$  intermediate as suggested in the literature.<sup>29,41</sup> This accounts for the enhanced superoxide transport which leads to the formation of larger  $\text{NaO}_2$  crystals with improved cell capacity.<sup>29</sup> Recently Aetukuri et al. suggested that  $\text{H}_2\text{O}$  acts as a solvating additive that drives the solution processes and enhances the growth of  $\text{Li}_2\text{O}_2$  toroids. As solvation does not change the surface ORR kinetics, it shows negligible influence on the overpotentials of  $\text{Li}-\text{O}_2$  cells.<sup>30</sup> In contrast, as shown in Figure 3b, the discharge overpotential of the  $\text{Na}-\text{O}_2$  cell is lowered by 100 mV when the  $\text{H}_2\text{O}$  concentration of electrolyte increases from 10 to 5000 ppm. Similar improvement is also observed in the RRDE studies of  $\text{Na}-\text{O}_2$  chemistry.<sup>29</sup> On the basis of cyclic voltammetry and *in situ* Raman studies on  $\text{Li}-\text{O}_2$  cells, Markovic et al. also concluded that  $\text{H}_2\text{O}$  acts as a catalyst and promoter, thus improving ORR by interacting with the superoxide species on the surface of the cathode.<sup>42</sup>

**ESR Evidence of Carbon-Centered Organic Radicals on Reduction.** When an ultrahigh  $\text{H}_2\text{O}$  concentration of 5000 ppm is added to the electrolyte, the ESR spectrum of the discharged electrolyte changes to a six-peak pattern. This pattern has very different underlying hyperfine values compared to the DMPO-OOH pattern, indicating the formation of other radicals (see Figure 3a). The hyperfine coupling constants of  $\alpha_{\text{N}} = 14.1\ \text{G}$  and  $\alpha_{\text{H}} = 21.3\ \text{G}$  indicate carbon-centered radicals (Figure S5).<sup>43</sup> Large amounts of hydroperoxyl, well-known as a chemically reactive radical, will cause hydrogen abstraction from the glyme solvent thus forming carbon-centered radicals as reported previously.<sup>12</sup> This results in the decomposition of

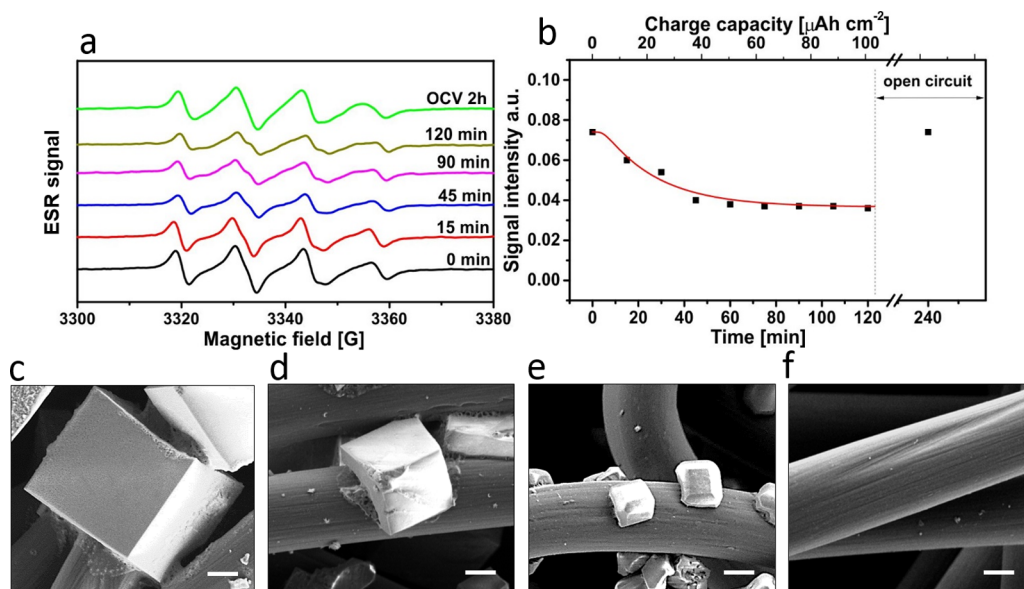


**Figure 4.** ESR spectra of the electrolyte at different charge depths (a) and the changes in intensity of DMPO-OOH signal upon charge (b). Black squares indicate the measured intensities, and the red line is the calculated intensity curve based on the solution-diffusion model. (c-f) Morphology of cathodes charged for 0 min (c), 90 min (d), 1200 min (e), and 3.5 V (~2160 min) (f). Note: the cathodes were pre-discharged to 2  $\text{mAh cm}^{-2}$  and were then used for charge studies. The white bars indicate a length of 5  $\mu\text{m}$ . The charge current is constant at 50  $\mu\text{A cm}^{-2}$ .

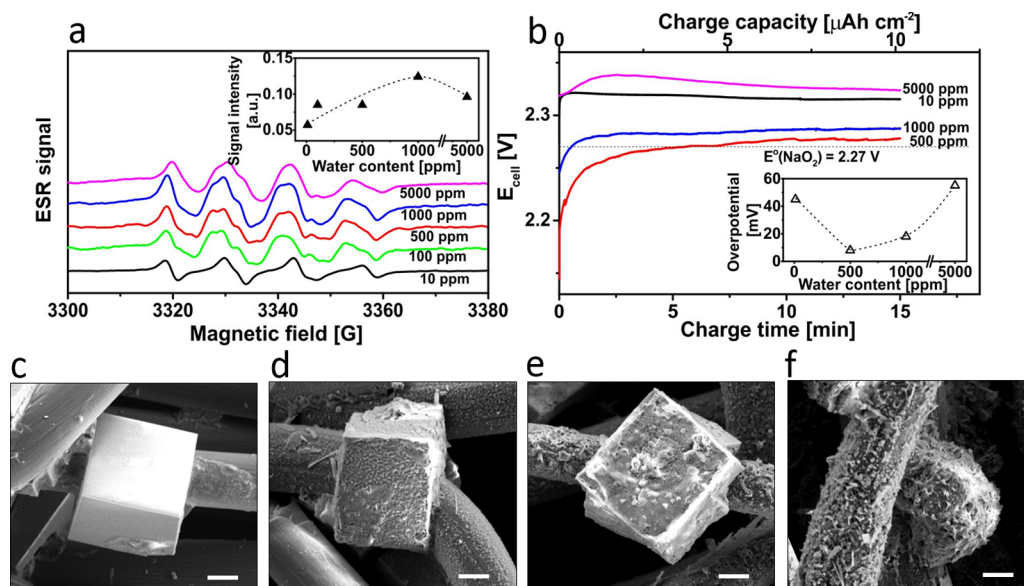


**Figure 5.** Effects of water concentrations on the ESR spectra of charged electrolytes (a) and the charge curves of Na-O<sub>2</sub> cells at a constant charge time of 15 min (b). Insets show the intensity changes of ESR signal from DMPO-OOH adducts and the charge overpotential changes of cells as a function of H<sub>2</sub>O content. (c-f) Morphology of cathodes charged for 15 min using electrolytes with H<sub>2</sub>O concentrations of 10 ppm (c), 500 ppm (d), 1000 ppm (e), and 5000 ppm (f), respectively. The white bars indicate a length of 5  $\mu\text{m}$ . A constant charge rate of 50  $\mu\text{A cm}^{-2}$  is applied.

electrolyte restricting the cycling performances of Na-O<sub>2</sub> cells.<sup>44</sup> Therefore, only low quantities of H<sub>2</sub>O (<5000 ppm) can be tolerated in Na-O<sub>2</sub> cells.

**Solution-Mediated NaO<sub>2</sub> Oxidation.** The reversible oxidation of NaO<sub>2</sub> products through solution-mediated transport determines the rechargeability of the Na-O<sub>2</sub> chemistry. For charging studies, carbon cathodes pre-discharged to 2  $\text{mAh cm}^{-2}$  were used. Prior to charge, reaction of the electrolyte containing 10 ppm of H<sub>2</sub>O with DMPO shows the ESR spectrum of the DMPO-OOH adduct (Figure 4a). Naturally, the HO<sub>2</sub> formed on discharge is not consumed (it is a catalyst). As presented in Figure 4b, upon charge, the intensity of

DMPO-OOH signal decreases and then reaches steady state after 45 min of charge. It indicates that the charge reaction consumes the superoxide in the electrolyte. We constructed a solution-diffusion model to simulate the charge processes, assuming that superoxide diffuses to the surface of the cathode, via electrolyte, for oxidation (see Figure S6 for modeling details). As shown in Figure 4b, the calculated signal-intensity curve (red curve) based on this model agrees well with the experimental results (black squares). In addition, this model also reveals that solvent properties, e.g., hydroperoxyl solubility and its diffusion coefficient, will significantly influence superoxide mobility in the electrolytes, which would in turn affect the

charge behavior of Na-O<sub>2</sub> cells (Figure S7). In comparison with the diglyme-based electrolyte, the ionic liquid 1-butyl-1-methylpyrrolidinium bis(trifluoromethanesulfonyl)imide (Pyr14TFSI) and tetraethylene glycol dimethyl ether (tetraglyme) exhibit lower superoxide solubilities and diffusion coefficients, thereby leading to high charge overpotentials and poor Coulombic efficiencies (see Figure S8).<sup>40,45</sup> In addition, shoulders appear in the ESR spectrum when the charge time is longer than 90 min, as shown in Figure 4a. These additional peaks indicate the formation of other radical species. They were also observed in the presence of large amounts of H<sub>2</sub>O (see above, Figure 3a) and identified as oxygen-centered organic radical species. Elucidation of their spectral features is presented near the end of the discussion. Upon the interruption of charge, NaO<sub>2</sub> crystals continuously dissolve in the electrolyte until an equilibrium state, i.e., maximum solubility, is achieved. The intensity of the DMPO-OOH adduct signal thus returns to its initial value after the cathode rests at open circuit conditions for 2 h (Figure 4b).

Figure 4c–f shows the morphology changes of the cathodic products upon charge. The dissolution of NaO<sub>2</sub> diminishes the size of the cubic crystals. At a charge time of 1200 min, the edges of NaO<sub>2</sub> particles are preferentially dissolved, likely due to their higher surface energy.<sup>46</sup> After charging the Na-O<sub>2</sub> cell up to 3.5 V, NaO<sub>2</sub> products are fully oxidized showing a bare cathode (see Figure 4f). The Na-O<sub>2</sub> cell shows a typical Coulombic efficiency of 90% due to parasitic reactions and loss of superoxide within the cell.<sup>47,48</sup>

**Effect of High Water Concentrations on Charge.** With increasing H<sub>2</sub>O concentration (up to 1000 ppm) larger ESR signals from the DMPO-OOH adduct are observed. This indicates more superoxide radicals are present in the electrolyte (Figure 5a). It also suggests that H<sub>2</sub>O improves the solubilization of superoxide during charge. Furthermore, the charge overpotential of the cell using an electrolyte with 500 ppm of H<sub>2</sub>O is ~30 mV lower than that of the electrolyte with 10 ppm of H<sub>2</sub>O (Figure 5b). However, when the H<sub>2</sub>O concentration is higher than 500 ppm, the charge overpotential rises. Figure 5c–f shows that the increase of H<sub>2</sub>O content roughens the surface of NaO<sub>2</sub> cubic crystals. The carbon fibers are fully covered with flake-like particles. These particles are identified as sodium acetate and sodium peroxide dihydrate byproducts (Figure S9). Thus, enhanced solubilization of superoxide triggers the decomposition of the electrolyte during charge. This is discussed below.

**ESR Evidence of Oxygen-Centered Organic Radicals on Oxidation.** Figure 6 compares the normalized ESR spectra of the electrolyte samples containing 10 ppm of H<sub>2</sub>O charged for 0 and 120 min as well as the electrolyte samples with 10 and 500 ppm of H<sub>2</sub>O charged for 15 min. The spectrum with either longer charge time or higher H<sub>2</sub>O concentration in the electrolyte presents a distorted ESR pattern compared with that of the DMPO-OOH adduct, which indicates another radical species is formed under these conditions. Subtraction of the sets of measured spectra shows identical ESR patterns of the newly formed radicals (blue curves) with six equally distanced peaks. The simulated ESR spectra (dotted magenta curves) with simulation parameters of  $\alpha_N = 12.8$  G and  $\alpha_H = 6.4$  G show good agreement to the subtracted spectra (more detailed analysis on the spectra is given in the SI). The extracted hyperfine coupling constants obtained from the simulations suggest that the paramagnetic species responsible for the

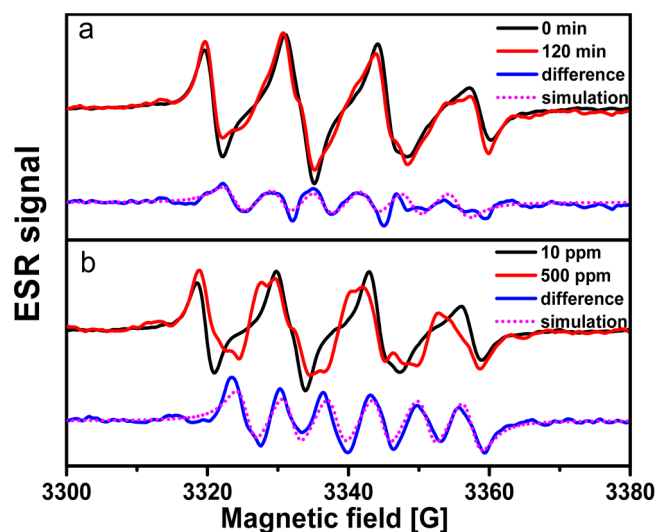


**Figure 6.** (a) Comparison of normalized ESR spectra of the electrolyte samples with 10 ppm of H<sub>2</sub>O charged for 0 min (black curve) and 120 min (red curve). The blue solid curve is the spectrum obtained by subtracting the ESR signal of 120 min charged electrolyte from that of 0 min charged electrolyte. The dotted magenta curve is the simulation of the subtracted spectrum. (b) Comparison of ESR spectra of the electrolyte samples containing 10 and 500 ppm of H<sub>2</sub>O charged for 15 min. The blue solid curve is the spectrum obtained by subtracting the ESR signal of charged electrolyte with 500 ppm of H<sub>2</sub>O from that of charged electrolyte with 10 ppm of H<sub>2</sub>O. Dotted magenta curve is the simulated spectrum.

observed signals are likely oxygen-centered alkyl radicals (RO<sup>•</sup>).<sup>32</sup>

Consistent with the results here, Adams et al. recently demonstrated that glyme-based solvents decompose and form alkyl oxygen radicals through hydrogen abstraction by superoxide followed by a  $\beta$ -scission.<sup>49</sup> The results in Figure 6 indicate that the formation of RO<sup>•</sup> radicals requires either longer charge or higher H<sub>2</sub>O content. Based on simulations, Khetan et al. suggested that the rate of solvent degradation is determined by the solvent acidity ( $pK_a$ ) and concentration of superoxide in the electrolyte.<sup>50</sup> With the electrolyte used here that contains 10 ppm H<sub>2</sub>O, a long time may be required to achieve a sufficiently high content of superoxide due to its limited dissolution rate. However, such concentration of superoxide could easily be obtained in the presence of large amounts of H<sub>2</sub>O. These solution processes greatly influence the reversibility of Na-O<sub>2</sub> cells.

We have demonstrated that these chemically unstable alkyl oxygen radicals further degrade to sodium acetate,<sup>51</sup> while superoxide is finally converted to Na<sub>2</sub>O<sub>2</sub>·2H<sub>2</sub>O via reaction of NaO<sub>2</sub> with water<sup>52</sup> upon peroxo-hydroxylation as proposed by Kim et al.<sup>53</sup> Upon charge, these insoluble byproducts progressively precipitate from the electrolyte, forming a passivating layer on the cathode (Figure 5c–f).<sup>51</sup> This raises the charge overpotential of Na-O<sub>2</sub> cells using electrolytes with high H<sub>2</sub>O content (Figure 5b).

Clearly, the reactivity of the HO<sub>2</sub> radical—formed in Na-O<sub>2</sub> and Li-O<sub>2</sub> cells alike in the presence of trace water—is a major problem underlying rechargeability. Work is needed to develop transfer agents to solubilize and stabilize sodium superoxide in the electrolyte (as recently demonstrated for the Li-O<sub>2</sub> system),<sup>54,55</sup> which would aid in preventing decomposition of aprotic solvents.



## CONCLUSIONS

Key to the findings presented here was coupling the technique of cold spin traps—to stabilize the dissolved superoxide species in the electrolyte for ESR analysis—with parallel investigations of the morphological evolution of solid NaO<sub>2</sub> products by SEM. The observation of the ESR signal of DMPO-HO<sub>2</sub> (i.e., DMPO-OOH) conclusively shows the solubilization of superoxide in the 10 ppm of H<sub>2</sub>O/diglyme-based electrolyte via hydroperoxyl radicals. Increasing H<sub>2</sub>O content leads to a greatly enhanced DMPO-OOH ESR signal, indicative of higher HO<sub>2</sub> concentration. Once a critical supersaturation is achieved, nucleation and growth of NaO<sub>2</sub> cubic crystals on the cathode, as observed by SEM, follow the classical LaMer mechanism. We propose this takes place by metathesis (HO<sub>2</sub> + Na<sup>+</sup> ⇌ NaO<sub>2</sub> + H<sup>+</sup>). On charge, the reverse occurs: The NaO<sub>2</sub> crystals shrink in size, while the diminished intensity of the DMPO-OOH signal indicates consumption of superoxide in the electrolyte. These findings show that the charge pathway involves the dissolution of NaO<sub>2</sub> and subsequent hydroperoxyl diffusion to the carbon cathode where it is oxidized; i.e., HO<sub>2</sub> → O<sub>2</sub> + H<sup>+</sup> + e<sup>-</sup>. A simple model to simulate the diffusion of the hydroperoxyl radical in the electrolyte and its electrochemical oxidation agrees very well with the changes in hydroperoxyl concentration as measured by the ESR signal intensity.

The results provide not only direct evidence of the soluble hydroperoxyl species in the Na-O<sub>2</sub> cell and its role in transport but also of its reaction with glyme to form both carbon-centered and oxygen-centered organic radicals. These are predicted to be the agents that degrade the electrolyte, lowering the charge efficiency and limiting the cycling capabilities of the Na-O<sub>2</sub> cells.<sup>51</sup> This provides insight into a significant reaction pathway. A better understanding into the solution-mediated oxygen reaction mechanism should inspire future studies to explore other phase transfer catalysts with higher efficiency and to develop chemically stable electrolytes, both liquid and solid.<sup>56–58</sup>

## ASSOCIATED CONTENT

### Supporting Information

The Supporting Information is available free of charge on the ACS Publications website at DOI: 10.1021/jacs.6b05382.

Experimental details, analysis of ESR spectra, modeling, characterization of cathodic products, and electrochemical testing of Na-O<sub>2</sub> cells (PDF)

## AUTHOR INFORMATION

### Corresponding Authors

\*baugh@uwaterloo.ca

\*lfnazar@uwaterloo.ca

### Notes

The authors declare no competing financial interest.

## ACKNOWLEDGMENTS

The authors acknowledge financial support from NRCan, through the EcoEII programme, and from NSERC, via the Canada Research Chair (to L.F.N.). We would like to acknowledge the NSERC Discovery programme (to L.F.N. and J.B.) and the Institute for Quantum Computing for support, and we also thank D. G. Cory for access to the ESR spectrometer. In addition, we thank the Canada Graduate Scholarships-Master's Program and the scholarship of Waterloo

Institute of Nanotechnology (to R.F.). Finally, the authors thank R. Black and N. Moghimi for SEM measurements and M. Mathew for discussion on the modelling.

## REFERENCES

- (1) Goodenough, J. B.; Park, K.-S. *J. Am. Chem. Soc.* **2013**, *135*, 1167–1176.
- (2) Girishkumar, G.; McCloskey, B.; Luntz, A. C.; Swanson, S.; Wilcke, W. *J. Phys. Chem. Lett.* **2010**, *1*, 2193–2124.
- (3) Ogasawara, T.; Débart, A.; Holzapfel, M.; Novák, P.; Bruce, P. G. *J. Am. Chem. Soc.* **2006**, *128*, 1390–1393.
- (4) Abraham, K. M. *J. Electrochem. Soc.* **1996**, *143*, 7.
- (5) Chen, Y.; Freunberger, S. A.; Peng, Z.; Bardé, F.; Bruce, P. G. *J. Am. Chem. Soc.* **2012**, *134*, 7952–7957.
- (6) Black, R.; Oh, S. H.; Lee, J.-H.; Yim, T.; Adams, B.; Nazar, L. F. *J. Am. Chem. Soc.* **2012**, *134*, 2902–2905.
- (7) Ganapathy, S.; Adams, B. D.; Stenou, G.; Anastasaki, M. S.; Goubitz, K.; Miao, X.-F.; Nazar, L. F.; Wagemaker, M. *J. Am. Chem. Soc.* **2014**, *136*, 16335–16344.
- (8) Radin, M. D.; Rodriguez, J. F.; Tian, F.; Siegel, D. J. *J. Am. Chem. Soc.* **2012**, *134*, 1093–1103.
- (9) Xia, C.; Waletzko, M.; Chen, L.; Pepler, K.; Klar, P. J.; Janek, J. *ACS Appl. Mater. Interfaces* **2014**, *6*, 12083–12092.
- (10) Kundu, D.; Black, R.; Adams, B.; Nazar, L. F. *ACS Cent. Sci.* **2015**, *1*, 510–515.
- (11) Bergner, B. J.; Schürmann, A.; Pepler, K.; Garsuch, A.; Janek, J. *J. Am. Chem. Soc.* **2014**, *136*, 15054–15064.
- (12) Freunberger, S. A.; Chen, Y.; Drewett, N. E.; Hardwick, L. J.; Bardé, F.; Bruce, P. G. *Angew. Chem., Int. Ed.* **2011**, *50*, 8609–8613.
- (13) McCloskey, B. D.; Speidel, A.; Scheffler, R.; Miller, D. C.; Viswanathan, V.; Hummelshøj, J. S.; Nørskov, J. K.; Luntz, A. C. *J. Phys. Chem. Lett.* **2012**, *3*, 997–1001.
- (14) Ottakam Thotiyl, M. M.; Freunberger, S. A.; Peng, Z.; Bruce, P. G. *J. Am. Chem. Soc.* **2013**, *135*, 494–500.
- (15) Freunberger, S. A.; Chen, Y.; Peng, Z.; Griffin, J. M.; Hardwick, L. J.; Bardé, F.; Novák, P.; Bruce, P. G. *J. Am. Chem. Soc.* **2011**, *133*, 8040–8047.
- (16) Vivek, J. P.; Berry, N.; Papageorgiou, G.; Nichols, R. J.; Hardwick, L. J. *J. Am. Chem. Soc.* **2016**, *138*, 3745–3751.
- (17) Liu, T.; Leskes, M.; Yu, W.; Moore, A. J.; Zhou, L.; Bayley, P. M.; Kim, G.; Grey, C. P. *Science* **2015**, *350*, 530–533.
- (18) Li, F.; Wu, S.; Li, D.; Zhang, T.; He, P.; Yamada, A.; Zhou, H. *Nat. Commun.* **2015**, *6*, 7843–7849.
- (19) Hartmann, P.; Bender, C. L.; Vračar, M.; Dürr, A. K.; Garsuch, A.; Janek, J.; Adelhalm, P. *Nat. Mater.* **2012**, *12*, 228–232.
- (20) Das, S. K.; Lau, S.; Archer, L. A. *J. Mater. Chem. A* **2014**, *2*, 12623–12629.
- (21) Bender, C. L.; Hartmann, P.; Vračar, M.; Adelhalm, P.; Janek, J. *Adv. Energy Mater.* **2014**, *4*, 1301863.
- (22) Lu, J.; Jung Lee, Y.; Luo, X.; Chun Lau, K.; Asadi, M.; Wang, H.-H.; Brombosz, S.; Wen, J.; Zhai, D.; Chen, Z.; Miller, D. J.; Sub Jeong, Y.; Park, J.-B.; Zak Fang, Z.; Kumar, B.; Salehi-Khojin, A.; Sun, Y.-K.; Curtiss, L. A.; Amine, K. *Nature* **2016**, *529*, 377–382.
- (23) Ren, X.; Wu, Y. *J. Am. Chem. Soc.* **2013**, *135*, 2923–2926.
- (24) Hartmann, P.; Bender, C. L.; Sann, J.; Dürr, A. K.; Jansen, M.; Janek, J.; Adelhalm, P. *Phys. Chem. Chem. Phys.* **2013**, *15*, 11661–11672.
- (25) Lee, B.; Kim, J.; Yoon, G.; Lim, H.-D.; Choi, I.-S.; Kang, K. *Chem. Mater.* **2015**, *27*, 8406–8413.
- (26) Hartmann, P.; Heinemann, M.; Bender, C. L.; Graf, K.; Baumann, R.-P.; Adelhalm, P.; Heiliger, C.; Janek, J. *J. Phys. Chem. C* **2015**, *119*, 22778–22786.
- (27) Bender, C. L.; Schröder, D.; Pinedo, R.; Adelhalm, P.; Janek, J. *Angew. Chem., Int. Ed.* **2016**, *55*, 4640–4649.
- (28) Ortiz-Vitoriano, N.; Batcho, T. P.; Kwabi, D. G.; Han, B.; Pour, N.; Yao, K. P. C.; Thompson, C. V.; Shao-Horn, Y. *J. Phys. Chem. Lett.* **2015**, *6*, 2636–2643.

- (29) Xia, C.; Black, R.; Fernandes, R.; Adams, B.; Nazar, L. F. *Nat. Chem.* **2015**, *7*, 496–501.
- (30) Aetukuri, N. B.; McCloskey, B. D.; García, J. M.; Krupp, L. E.; Viswanathan, V.; Luntz, A. C. *Nat. Chem.* **2014**, *7*, 50–56.
- (31) Villamena, F. A.; Merle, J. K.; Hadad, C. M.; Zweier, J. L. *J. Phys. Chem. A* **2005**, *109*, 6089–6098.
- (32) Pieta, P.; Petr, A.; Kutner, W.; Dunsch, L. *Electrochim. Acta* **2008**, *53*, 3412–3415.
- (33) Cao, R.; Walter, E. D.; Xu, W.; Nasybulin, E. N.; Bhattacharya, P.; Bowden, M. E.; Engelhard, M. H.; Zhang, J.-G. *ChemSusChem* **2014**, *7*, 2436–2440.
- (34) Rosen, G. M.; Rauckman, E. J. *Mol. Pharmacol.* **1980**, *17*, 233–238.
- (35) Harbour, J. R.; Hair, M. L. *J. Phys. Chem.* **1978**, *82*, 1397–1399.
- (36) Sugimoto, T. *Colloids Surf., A* **2000**, *164*, 183–204.
- (37) Vreeland, E. C.; Watt, J.; Schober, G. B.; Hance, B. G.; Austin, M. J.; Price, A. D.; Fellows, B. D.; Monson, T. C.; Hudak, N. S.; Maldonado-Camargo, L.; Bohorquez, A. C.; Rinaldi, C.; Huber, D. L. *Chem. Mater.* **2015**, *27*, 6059–6066.
- (38) LaMer, V. K.; Dinegar, R. H. *J. Am. Chem. Soc.* **1950**, *72*, 4847–4854.
- (39) Thanh, N. T. K.; Maclean, N.; Mahiddine, S. *Chem. Rev.* **2014**, *114*, 7610–7630.
- (40) Herranz, J.; Garsuch, A.; Gasteiger, H. A. *J. Phys. Chem. C* **2012**, *116*, 19084–19094.
- (41) Roberts, J. L.; Sawyer, D. T. *Isr. J. Chem.* **1983**, *23*, 430–438.
- (42) Staszak-Jirkovský, J.; Subbaraman, R.; Strmcnik, D.; Harrison, K. L.; Diesendruck, C. E.; Assary, R.; Frank, O.; Kopr, L.; Wiberg, G. K. H.; Genorio, B.; Connell, J. G.; Lopes, P. P.; Stamenkovic, V. R.; Curtiss, L.; Moore, J. S.; Zavadil, K. R.; Markovic, N. M. *ACS Catal.* **2015**, *5*, 6600–6607.
- (43) Buettner, G. R. *Free Radical Biol. Med.* **1987**, *3*, 259–303.
- (44) Zhao, N.; Guo, X. *J. Phys. Chem. C* **2015**, *119*, 25319–25326.
- (45) Johnson, L.; Li, C.; Liu, Z.; Chen, Y.; Freunberger, S. A.; Ashok, P. C.; Praveen, B. B.; Dholakia, K.; Tarascon, J.-M.; Bruce, P. G. *Nat. Chem.* **2014**, *6*, 1091–1099.
- (46) Lee, B.; Seo, D.-H.; Lim, H.-D.; Park, I.; Park, K.-Y.; Kim, J.; Kang, K. *Chem. Mater.* **2014**, *26*, 1048–1055.
- (47) McCloskey, B. D.; Garcia, J. M.; Luntz, A. C. *J. Phys. Chem. Lett.* **2014**, *5*, 1230–1235.
- (48) Bi, X.; Ren, X.; Huang, Z.; Yu, M.; Kreidler, E.; Wu, Y. *Chem. Commun.* **2015**, *51*, 7665–7668.
- (49) Adams, B. D.; Black, R.; Williams, Z.; Fernandes, R.; Cuisinier, M.; Berg, E. J.; Novak, P.; Murphy, G. K.; Nazar, L. F. *Adv. Energy Mater.* **2015**, *5*, 1400867.
- (50) Khetan, A.; Luntz, A.; Viswanathan, V. *J. Phys. Chem. Lett.* **2015**, *6*, 1254–1259.
- (51) Black, R.; Shyamsunder, A.; Adeli, P.; Kundu, D.; Murphy, G.; Nazar, L. F. *ChemSusChem* **2016**, *9*, 1795–1803.
- (52) Zhao, N.; Li, C.; Guo, X. *Phys. Chem. Chem. Phys.* **2014**, *16*, 15646–15652.
- (53) Kim, J.; Park, H.; Lee, B.; Seong, W. M.; Lim, H.-D.; Bae, Y.; Kim, H.; Kim, W. K.; Ryu, K. H.; Kang, K. *Nat. Commun.* **2016**, *7*, 10670–10677.
- (54) Gao, X.; Chen, Y.; Johnson, L.; Bruce, P. *Nat. Mater.* **2016**, *15*, 882–888.
- (55) Kwak, W. J.; Hirshberg, D.; Sharon, D.; Afri, M.; Frimer, A. A.; Jung, H. G.; Aurbach, D.; Sun, H.-K. *Energy Environ. Sci.* **2016**, *9*, 2334–2345.
- (56) Giordani, V.; Tozier, D.; Tan, H.; Burke, C. M.; Gallant, B. M.; Uddin, J.; Greer, J. R.; McCloskey, B. D.; Chase, G. V.; Addison, D. J. *Am. Chem. Soc.* **2016**, *138*, 2656–2663.
- (57) Zhu, X. B.; Zhao, T. S.; Wei, Z. H.; Tan, P.; An, L. *Energy Environ. Sci.* **2015**, *8*, 3745–3754.
- (58) Walker, W.; Giordani, V.; Uddin, J.; Bryantsev, V. S.; Chase, G. V.; Addison, D. J. *Am. Chem. Soc.* **2013**, *135*, 2076–2079.